ALMA MATER STUDIORUM
UNIVERSITÀ DI BOLOGNA

ARCHIVIO ISTITUZIONALE
DELLA RICERCA

Alma Mater Studiorum Università di Bologna
Archivio istituzionale della ricerca

Three-dimensional simulation of hydraulic fracture propagation height in layered formations

This is the final peer-reviewed author's accepted manuscript (postprint) of the following publication:

Published Version:
Zhao K., Stead D., Kang H., Gao F., Donati D. (2021). Three-dimensional simulation of hydraulic fracture propagation height in layered formations. ENVIRONMENTAL EARTH SCIENCES, 80(12), --- [10.1007/s12665-021-09728-x].

Availability:
This version is available at: https://hdl.handle.net/11585/837010 since: 2024-01-18

Published:
DOI: http://doi.org/10.1007/s12665-021-09728-x

Terms of use:

Some rights reserved. The terms and conditions for the reuse of this version of the manuscript are specified in the publishing policy. For all terms of use and more information see the publisher's website.

This item was downloaded from IRIS Università di Bologna (https://cris.unibo.it/).
When citing, please refer to the published version.

(Article begins on next page)

27 August 2024

Three-dimensional numerical investigation of the interaction between multiple hydraulic fractures in horizontal wells

Kaikai Zhao[a,b], Doug Stead[c], Hongpu Kang[a,b], Fuqiang Gao[a,b,*], Davide Donati[c]

[a] State Key Laboratory of Coal Mining and Clean Utilization (China Coal Research Institute), Beijing, China

[b] Mining & Designing Branch, China Coal Research Institute, Beijing, China

[c] Engineering Geology and Resource Geotechnics, Simon Fraser University, Burnaby, BC, Canada

[*] Corresponding author: fuqgao@gmail.com (F. Gao).

Abstract

Complex, non-planar fracture geometry is often observed in multi-stage hydraulic fracturing. The opening of hydraulic fractures results in a disturbance of local stress, which in turn affects the propagation of the adjacent fractures (stress shadow effect). The interaction between multiple fractures is of major importance in the design of fracturing treatments. In this study, a fullycoupled three-dimensional lattice-spring code is utilized to study the interference among multiple fractures. The results indicate that simultaneous propagating fractures can move towards or away from each other, resulting in complicated non-planar geometry and branching of hydraulic fractures. In an isotropic stress field, continued fracture propagation involves reorientation into a direction normal to the initial fracture plane, leading to an S-shaped fracture geometry. Higher Young's modulus values amplify the interaction of multiple fractures, resulting in more secondary fractures normal to the initial fracture plane and the greater dimension of fracture. Treatments assuming a higher magnitude of fluid viscosity /injection rate induce more branches at the tips of the primary fracture. An adjacent layer with a low modulus restricts the height growth of fractures, whereas the lateral growth and the stress interference will be in contrast relatively enhanced. This study provides further insight into the design and optimization of multiple-stage hydraulic fracturing in horizontal wells.

Keywords: Stress shadow, Hydraulic fracturing, In-situ stress, Young's modulus, Hydro-mechanical coupling, Lattice spring modeling

1. Introduction

Hydraulic fracturing has been extensively applied to the oil and gas industry [1], Enhanced Geothermal Systems [2], and the mining industry [3]. Complex, non-planar hydraulic fracture (HF) geometry is often observed in multi-stage hydraulic fracturing in horizontal wells. The interaction of multiple HFs is of major importance in the routine design of well completions and treatment strategies. The opening of an HF causes an alteration in the neighboring stress field, which in turn affects the propagation of the adjacent HFs. This phenomenon is referred to as the "stress shadow effect" [1]. Green and Sneddon [4] presented an analytical solution for a pressurized HF opening and the induced stress in an elastic solid. Based on Green and Sneddon's solution, an

analysis of the fracture-induced stresses has been given to calculate the stability of reservoirs [5]. A three-dimensional stress solution produced by an elliptical crack has also been developed [6]. However, calculating stress variations induced by the interaction between multiple curved HFs using analytical solutions remains a challenging task.

Stress shadow has been documented for decades from fracture mapping data. Field observation has shown that the maximum increase in compressive stress can be expected to occur at the HF plane, with the stress disturbance radiating into the surrounding rock for hundreds of feet [1]. Laboratory experiments showed that the stress shadow effect is evident with the presence of closely spaced notches [7]. The stress shadow effect may either inhibit the propagation of neighboring HFs or induce a deviation of neighboring HFs. An older HF impact the shape and path of newer HF. The newer HF path curved toward and coalesced with the older HF [8]. Because of experimental limitations, it is difficult to perform a sensitivity study of the stress interference process for multiple fracture propagation under laboratory conditions.

Numerical simulation has been extensively used to study the interaction between multiple HFs. A comprehensive overview of numerical methods for hydraulic fracturing can be found in previous publications [9–11]. Only a few numerical methods are introduced in this study, including the finite element method (FEM), boundary element method (BEM), displacement discontinuity method (DDM), distinct element method (DEM), and lattice spring method. A finite-element model has been employed to study the interaction between multiple HFs [12]. The results showed that the stress induced by the opening of the HF or the fluid leak-off could alter the magnitudes and orientations of the principal stresses, thereby influencing the pathway of the HF. The 3D multiple-cluster fracturing problems have been investigated using the XFEM-based CZM (cohesive zone model based on the extended FEM) [13]. Results showed that the HF propagation pathway depends on a complex stress distribution (or stress shadowing effect). The interaction between HFs causes HF to coalesce, grow parallel, or diverge depending on cluster spacing. A pseudo-3D model based on the BEM has been utilized to investigate the simultaneous growth of multiple HFs [14]. The simulations showed that the HFs do not always propagate perpendicular to the far-field, minimum principal stress direction. The HF pattern complexity is influenced by the magnitude of the HF net pressure relative to the differential stress. The interaction between multiple neighboring cracks has been investigated using the BEM model [15]. Modeling results showed that the creation of outer cracks could act to either promote or inhibit adjacent cracks propagation depending on the spacing and the loading conditions. A plane strain simulator based on the DDM has been developed for simulating multiple HFs growth [16]. The simulations showed that the HFs can curve toward or away from one another, potentially intersecting. The curving of HFs is associated with a combination of opening and sliding along the previous HF, as well as the disturbance of the local stress field. An HF-propagation model based on the DDM has been presented [17]. Model results indicated that non-planar geometry reduced propagation occurs for interior HFs, resulting in a substantial restriction in HF aperture and a reduction in length. A pseudo 3D-based HF model based on the 3D-DDM has been developed [18]. Model results showed that the height growth may be promoted or suppressed for parallel HFs. The accurate prediction on the HF height and width profile require the incorporation of stress shadow effect.

The DEM has been extensively applied in different practices in rock engineering [19–21]. Simulations of stress interference among multiple HFs based on the DEM has been presented [22]. Simulation results showed that stress interference might impact the extent of the induced HF and treatment effectiveness. Numerical investigation of the stress shadow effect using the DM code (both mechanical only and hydro-mechanical coupled modes) has been presented [23]. The results showed that multiple HFs enhance the increase in minimum principal stress in the inter-fracture zone. Additionally, the increase in minimum principal stress reduces the HF apertures.

In the conventional DEM, discontinuities are regarded as distinct boundaries between blocks. The failure of intact blocks and the propagation of HFs may be simulated by implementing a Voronoi or Trigon tessellation within the intact blocks [24,25]. Therefore, the HF trajectory is constrained by the geometry of the contacts. Based on Synthetic Rock Mass and Lattice methods, a fully-coupled code, XSite, has been presented, which allows simulating asymmetrical non-planar HF propagation in a full 3D setting [26]. The simulation of non-planar propagation of multiple HFs using XSite has been presented [27]. Simulation results revealed that the propagation of a middle HF is enhanced with an increase in the cluster spacing but decreases for higher in-situ stress difference. The mechanical interference among multiple HFs has been investigated using XSite [28]. The simulation captured the HF front segmentation and asymmetric growth due to the combined influence of the stress shadowing and perforation/in-situ stress misalignment.

In the present study, the lattice simulator, XSite, is employed to study the interference between multiple HFs. The simulator allows sensitivity analyses of the key parameters influencing multiple HFs propagation to be undertaken. Several simulations of simultaneous propagation of multiple HFs are presented, in which the effects of the various parameters (in-situ stresses, Young's modulus (E), the viscosity of the fluid (μ), and injection rate (Q)) are investigated. Multiple HFs propagation in a layered formation is also simulated.

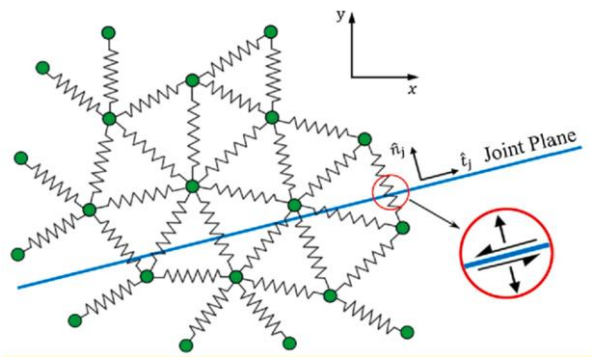

Fig. 1. Schematic representation of lattice array (after [30]).

2. Modeling methodology

The lattice method is developed based on the DEM, with particles and contacts replaced by nodes and springs, respectively. As shown in Fig. 1, the lattice is a quasi-random array of nodes connected by normal and

shear springs, which can fail in a brittle manner. The springs represent the elasticity of the rock mass. The fracturing of the intact material can be modeled by spring breakage. The joints can be inserted into the lattice spring network using a smooth joint model approach [26]. In XSite, the HF pathway is not predetermined but is part of the solution (for an accurate prediction of non-planar HF trajectory), and full deformation and stress are calculated (for an accurate prediction of the stress shadow) [29].

2.1. Modeling methodology

The model uses an explicit numerical solution to solve the motion of the lattice nodes. The central difference method is used to calculate the transitional degrees of freedom [26]:

$$\dot{u}_i^{(t+\Delta t/2)} = \dot{u}_i^{(t-\Delta t/2)} + \sum F_i^{(t)} \Delta t / m \tag{1}$$

$$u_i^{(t+\Delta t)} = u_i^{(t)} + \dot{u}_i^{(t+\Delta t/2)} \Delta t \tag{2}$$

where u˙(t)i and u(t)i are the velocity and position of component i at time t. m is the node mass, Δt is the time step,ΣF(t)i is the sum of all the force-components.

The angular velocities of component i at time t are calculated using Eq (3):

$$\omega_i^{(t+\Delta t/2)} = \omega_i^{(t-\Delta t/2)} + \frac{\sum M_i^{(t)}}{I} \Delta t \tag{3}$$

where ωi is the angular velocity of component i(i = 1,3) at time t, and ΣMi is the sum of all moment-components acting on the node of the moment of inertia, I.

Spring force variation and relative displacement are calculated by the velocities of the nodes [26]:

$$F^N \leftarrow F^N + \dot{u}^N k^N \Delta t \tag{4}$$

$$F_i^S \leftarrow F_i^S + \dot{u}_i^S k^S \Delta t \tag{5}$$

where F is the force, k is the stiffnesses, “N” and “S” represents normal and shear, respectively. u˙Nand u˙iS are the velocity of component i in the normal and shear directions, respectively. The spring will break and micro-crack will form if the spring force exceeds the calibrated spring strength.

2.2. Fluid flow formulation

Fluid flow is simulated by the pipes network that connects fluid elements. As shown in Fig. 2, the fluid elements act as microcracks positioned at the broken spring or springs intersected by the joints. The pressures are stored in the fluid elements. Pipes are formed between the fluid elements within a certain distance between each other. As the microcracks are created, due to the breaking of the lattice springs as dictated by the forces in the lattice, the code automatically creates new fluid nodes and connects them, using flow pipes [26].

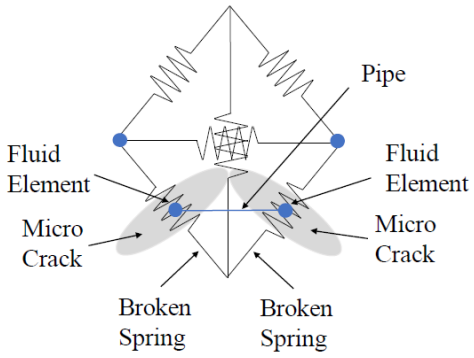

Fig. 2. Schematic representation of the pipe network (After [26]).

The flow rate along the pipe is calculated based on lubrication theory [31]:

$$q = \beta k_r \frac{a^3}{12\mu_f}[p^A - p^B + \rho_w g(z^A - z^B)] \tag{6}$$

where a is aperture, μf is fluid viscosity, pA and pBare hydraulic pressures at nodes “A” and “B”, respectively, zA and zB are elevations of nodes “A” and “B” respectively, ρw is fluid density, and g is gravitational acceleration. Calibration parameter β is applied to relate the joint conductivity to the conductivity of a pipe network. kr is the relative permeability, which depends on saturation, s:

$$k_r = s^2(3 - 2s) \tag{7}$$

The pressure increment with a timestep of Δt can be calculated as:

$$\Delta p = \frac{Q}{V} k_f \Delta t \tag{8}$$

where kf is the fluid bulk modulus, V is the volume of a fluid element.

$$Q = \sum_i q_i \tag{9}$$

is the sum of all flow rates, qi, from the pipes linked to the fluid element.

2.3. Fracture propagation criterion

criterion for HF propagation based on the J-integral is employed in XSite. The domain expression for local energy release rate at the crack front, in the direction of unit vector n, under quasi-static conditions, and assuming body force, Fi and traction T, on the crack faces, the J-integral is determined by the following relation [31]:

$$J = \frac{1}{R}\int_V [(\sigma_{ij}u_{ij} - W\delta_{ki})q_{,i}\hat{r} n_k - F_i u_{i,j}\hat{q^r} n_j]\mathrm{d}V - \frac{1}{R}\int_s T_j u_{j,k}\hat{q^r} n_k \mathrm{d}S \tag{10}$$

where R is the half-length of crack, W is strain energy density,V is a domain that includes the crack front, σ is the Cauchy stress tensor; u is the displacement vector, S is the fracture face, q̂r is a sufficiently smooth function.

q̂r is calculated as [31]:

$$\text{If } |\hat{r}| < 1, \hat{q^r} = 1 - \hat{r}, \text{ else } \hat{q^r} = 0 \tag{11}$$

where $\hat{r} = \sqrt{\hat{x_1}^2 + \hat{x_2}^2 + \hat{x_3}^2}$ (12)

$$\hat{x_i} = \frac{x_i - x_i^c}{R} \tag{13}$$

wherexi is the point coordinates at the arbitrary location, xc i is the point coordinates at centre of the spherical domain.

The stress intensity factor, K_I, is calculated as:

$$K_I = \sqrt{JE}$$

(14)

The fracture-propagation criteria rest on the principle that the integral in Eq. (10) is "zero" if no stress amplification is detected, otherwise provides a measure of stress intensity at the target location. Each spring in the model is tested as a potential location for the crack-propagation front. The integral in Eq. (10) is evaluated at the spring location in two directions, normal to each other, in a plane perpendicular to the spring. The maximum value of the two calculated values is taken as a measure of stress intensity (local energy release rate, J). If no stress amplification is detected (i.e., if $K_I << K_Ic$), spring tensile strength is used as the criterion for spring failure (i.e., it is compared to spring normal force); otherwise, the stress intensity factor is compared to rock toughness, KIc , to detect spring failure [31].

2.4. Coupling scheme

The coupling of mechanical deformation and fluid flow is incorporated in the code. The deformation and strength of the solid model depend on the fluid pressure. Fluid pressure is affected by solid deformation. Fracture permeability is determined by the HF aperture and the mechanical deformation [26].

3. Model description

Fig. 3 depicts the setup of the base model, the volume of the rock block was assumed as 5 m × 4 m × 4 m. A vertical starter crack (2) is positioned at the center of the block, normal to the x-axis. The starter cracks (1) and (3) are placed on the two sides of starter crack (2), and the distance between two adjacent cracks is 1.5 m. All starter crack has a radius of 0.2 m. Base model input parameters are listed in Table 1.

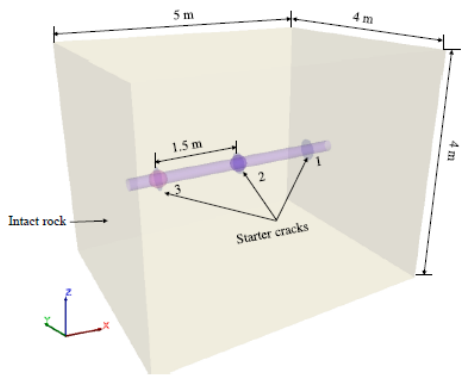

Fig. 3. Base model setup.

Table 1. Base model input parameters.

Variables	**Values**
ρ (kg/m3)	2650
Young's modulus, E (GPa)	20
Poisson's ratio, ν	0.25
Tensile strength, σt (MPa)	10
UCS, σc (MPa)	200
Permeability, (m2)	1×10^{-13}

4. Model results

4.1. Effect of in-situ stress

Three types of stress regime were considered, i.e. $\sigma x = \sigma y = \sigma z = 5$ MPa; $\sigma y = \sigma z = 5$ MPa, $\sigma x = 7.5$ MPa; $\sigma x = \sigma y = 5$ MPa, $\sigma z = 7.5$ MPa. Other parameters were assumed as: E = 20 GPa, $\mu = 1$ mPa·s. Simulations were conducted under a constant injection rate of 0.001 m3/s for 2 s.

For the case of $\sigma x = \sigma y = \sigma z = 5$ MPa (i.e., an isotropic stress field), in the very early stage of injection, three HFs perpendicular to the wellbore was initiated from the vertical starter cracks. The further propagation of the HFs was affected by the interaction between adjacent HFs, leading to an S-shaped fracture geometry (front view in Fig. 4). In general, the HFs were deflected into the direction of σx for the case of $\sigma x = \sigma y = \sigma z = 5$ MPa. These HFs are characterized by non-planar geometry and asymmetric propagation.

For the case of $\sigma x = 7.5$ MPa and $\sigma y = \sigma z = 5$ MPa, a preferred propagation direction of HFs became more evident. The HFs reorient themselves to become parallel to the horizontal plane (or normal to the direction of σz). The continued propagation pathway of the HFs was along the direction of σx. The maximum vertical growth of HFs was reduced compared to that for the case of $\sigma x = \sigma y = \sigma z = 5$ MPa.

For the case of $\sigma x = \sigma y = 5$ MPa and $\sigma z = 7.5$ MPa, the general propagation pathway of the HF 3 was along the direction of σz (i.e., perpendicular to the direction of σx), and the tilting of the HF plane was less evident than for the case of $\sigma x = \sigma y = \sigma z = 5$ MPa. The HF 2 was characterized by a bowl-shaped geometry, which deviated away from HF 3. Additionally, a noticeable secondary fracture was induced on the primary HF 1. The secondary fracture plane was simulated perpendicular to the direction of σy, whereas the main part of HF 1 was perpendicular to the direction of σx. HF 2 was simulated in an orthogonal direction to HF 1 (in the direction of σx) and propagated towards HF 2. The adjacent HF 1 and HF 2 progressively propagated away from each other, inducing an evident bowl shape in HF 1 in the early simulation stage, prior to the formation of the secondary fracture later during the simulation.

Fig. 5 present the vertical profiles of multiple HFs in the different stress regimes. Fracture deflection angle was introduced to quantitative evaluate the variation in fracture shape. Fracture deflection angle in the vertical direction is defined as the angle between the direction of σz and the tangent to the crack tip at the injection point. As shown in Fig. 5, each fracture has a deflection angle of more than 44◦ for the case of $\sigma x = \sigma y = \sigma z = 5$ MPa.

A much larger fracture deflection angle (greater than 60◦) can be found in the case of $\sigma x = 7.5$ MPa and $\sigma y = \sigma z = 5$ MPa. For the case of $\sigma x = \sigma y = 5$ MPa and $\sigma z = 7.5$ MPa, all three fracture has a relative straight pathway in the vertical direction. The fractures prefer to propagate in the direction of maximum principal stress.

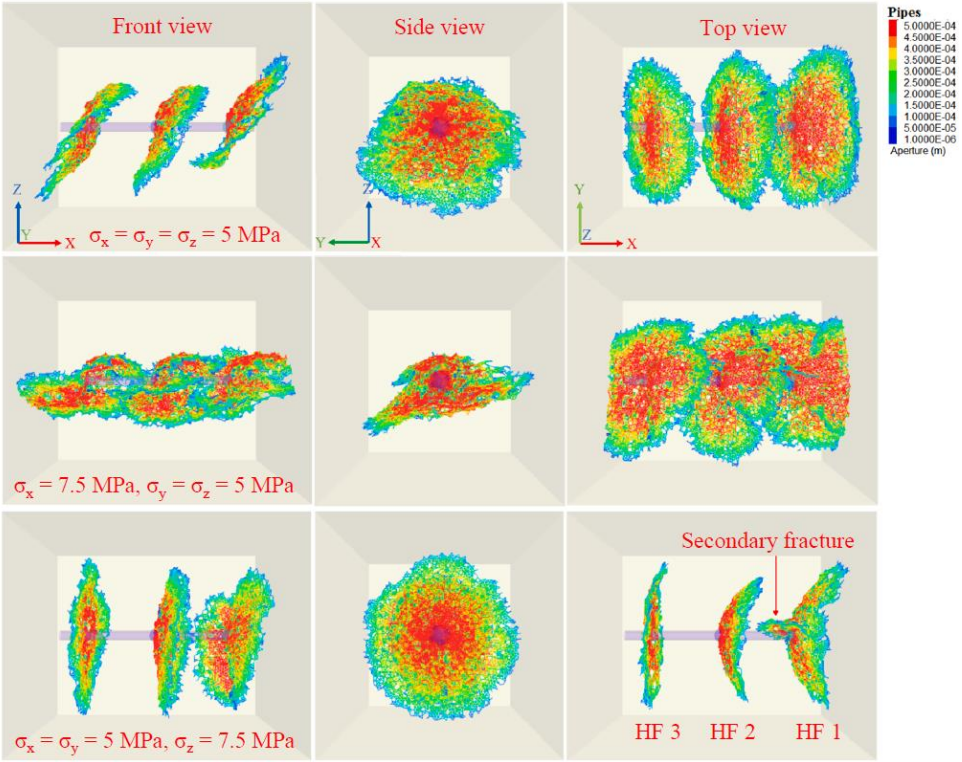

Fig. 4. Simultaneous growth of multiple HFs in the different stress regimes (The HF aperture was truncated at 0.001 mm and 0.5 mm).

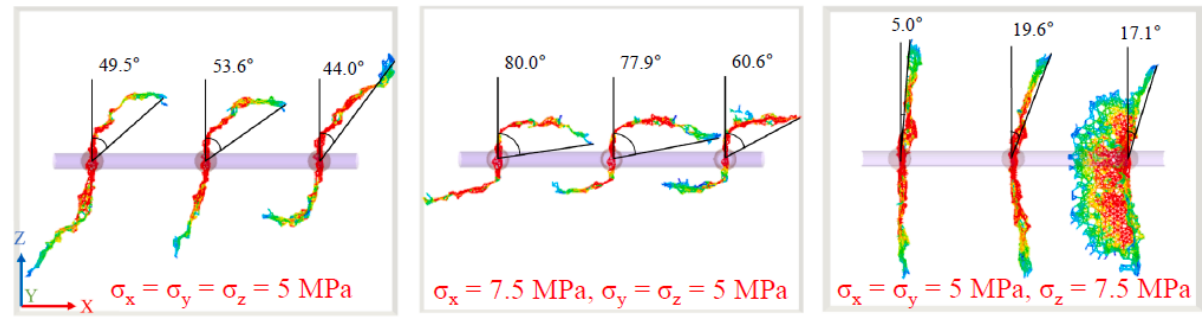

Fig. 5. Vertical profiles of multiple HFs in the different stress regimes.

4.2. Effect of Young's modulus

For the four models, the input modulus (E) was assumed as 5 GPa, 15 GPa, 20 GPa, and 30 GPa, respectively. Other parameters were assumed as: σx = σy = 5 MPa, σz = 7.5 MPa, μ = 1 mPa·s. Simulations were conducted under a constant injection rate of 0.001 m3/s for 2 s.

Fig. 6 shows the geometry of the HFs with varying modulus. With a low modulus of E = 5 GPa and 15 GPa, no secondary fracture was observed on the primary HF 1. For E = 20 GPa, a small secondary fracture induced on the primary HF 1. When E = 30 GPa was assumed, secondary fractures formed on both HF 1 and HF 2. Additionally, the dimension of secondary fracture in case of E = 30 GPa is greater than that of E = 20 GPa. In general, the curvature of the primary HFs increased with Young's modulus (refer to the top view for varying Young's

modulus). With E = 5 GPa, the shape of all three HFs is planar or sub-planar, with a less evident curvature compared to the other models. The bowl-shaped HFs were observed in cases with higher modulus values.

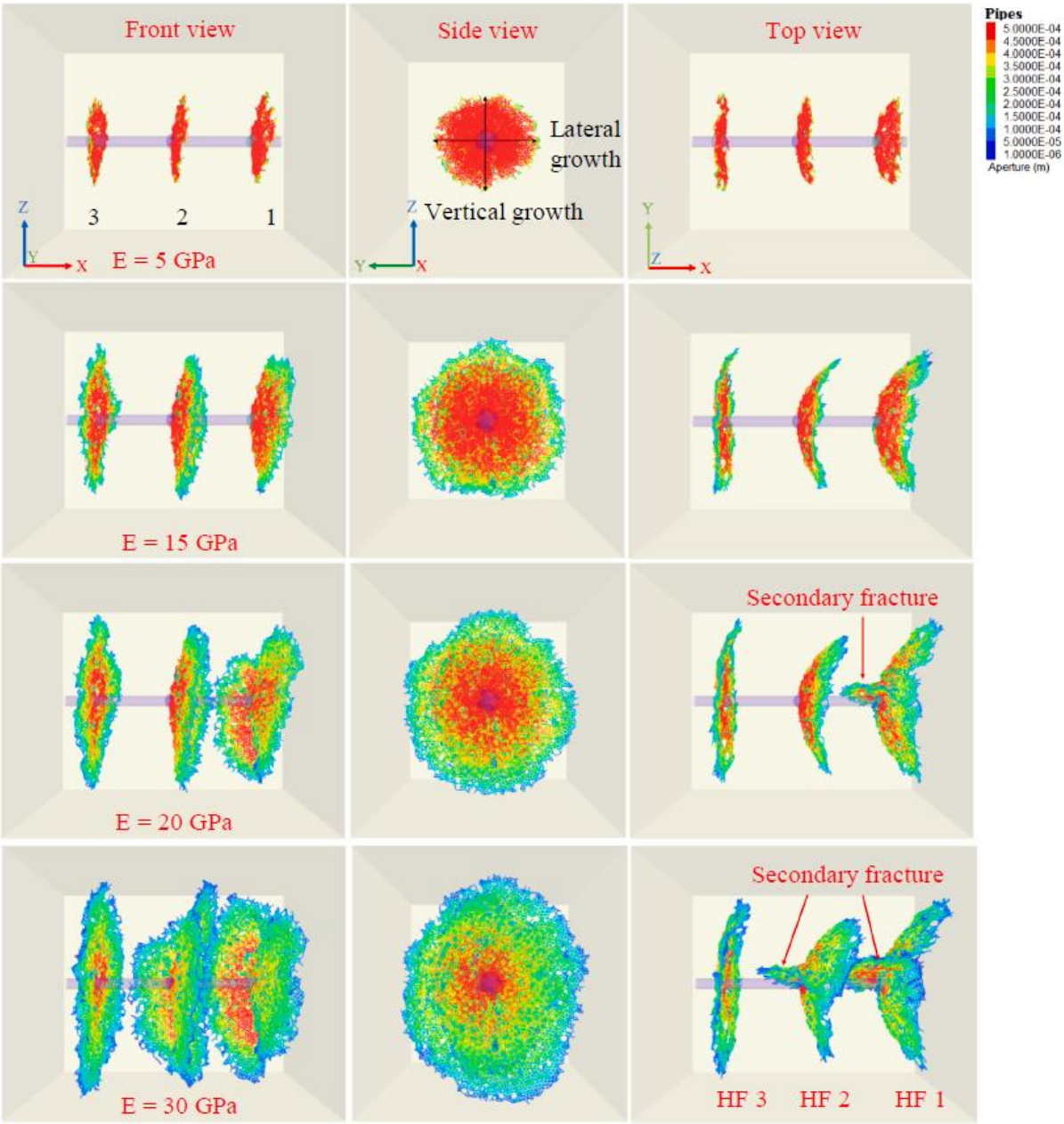

Fig. 6. Simultaneous growth of multiple HFs for varying Young's modulus.

Fig. 7 present the horizontal profiles of multiple HFs for varying Young's modulus. Fracture deflection angle in the horizontal direction is defined as the angle between the direction of σy and the tangent to the fracture tip at the injection point. As Young's modulus changed from 5 GPa to 15 GPa, the deflection angle in each fracture is promoted. For the case of E = 15 GPa, 20 GPa, and 30GPa, no marked variation in fracture deflection angle can be observed. The most evident difference is the propagation of secondary fracture. High Young's modulus contributes to the growth of secondary fractures. Those secondary fractures tend to be perpendicular to the initial fracture plane.

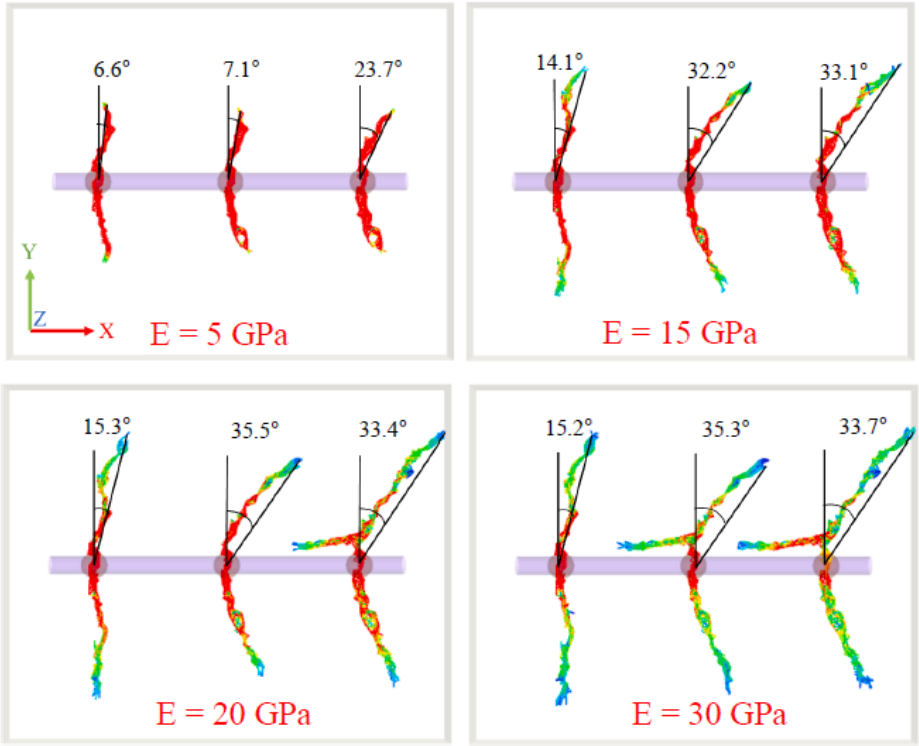

Fig. 7. Horizontal profiles of multiple HFs for varying Young's modulus.

Fig. 8 shows the vertical and lateral growth of HF 3 with changes in Young's modulus. The size (vertical and lateral growth) of the HF increased with an increase in modulus, assuming a constant injection rate.

Both vertical and lateral growth showed an increasing trend with the increase of Young's modulus. As Young's modulus increased from 5 GPa to 30 GPa, the vertical growth increased from 1.59 m to 3.83 m (+2.24 m), and the lateral growth increased from 1.72 m to 3.12 m (+1.4 m). The maximum difference between the vertical and lateral growth occurred in the case of E = 30 GPa with a magnitude of 0.71 m.

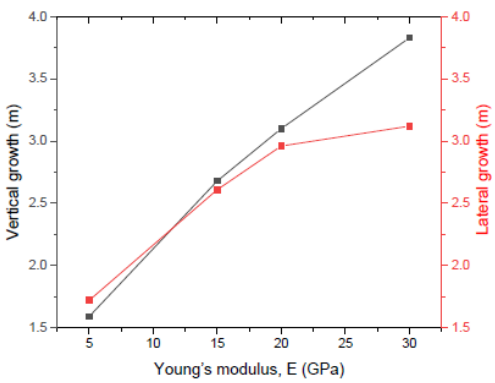

Fig. 8. Effect of Young's modulus on the vertical and lateral growth of HF 3.

Additionally, a marked variation in the HF aperture can be observed with changes in Young's modulus. Specifically, the main part of the HF aperture was greater than 0.5 mm for the case of E = 5 GPa, as shown in Fig. 6. For the case of E = 30 GPa, there was a relatively small region with an aperture greater than 0.5 mm around the injection point, whereas most parts of HF 3 had an aperture of lower than 0.5 mm.

4.3. Effect of the fluid viscosity

Four simulations were conducted with assumed fluid viscosity of 1, 3, 7, and 9 mPa·s, respectively. Other parameters were assumed as: σx = σy = 5 MPa, σz = 7.5 MPa, E = 20 GPa. Simulations were performed under a constant injection rate of 0.001 m3/s for 2 s.

As shown in Fig. 9, a secondary fracture can be observed for the cases of μ = 1 mPa·s and 3 mPa·s. With a higher fluid viscosity of μ = 7 mPa·s and 9 mPa·s, more induced branches occurred on the primary HF. Note that the secondary fracture under low fluid viscosity case of μ = 1 mPa·s was developed in the vicinity of the injection point. In contrast, branches for the high fluid viscosity case of μ = 9 mPa·s was observed at the tips of the primary fracture.

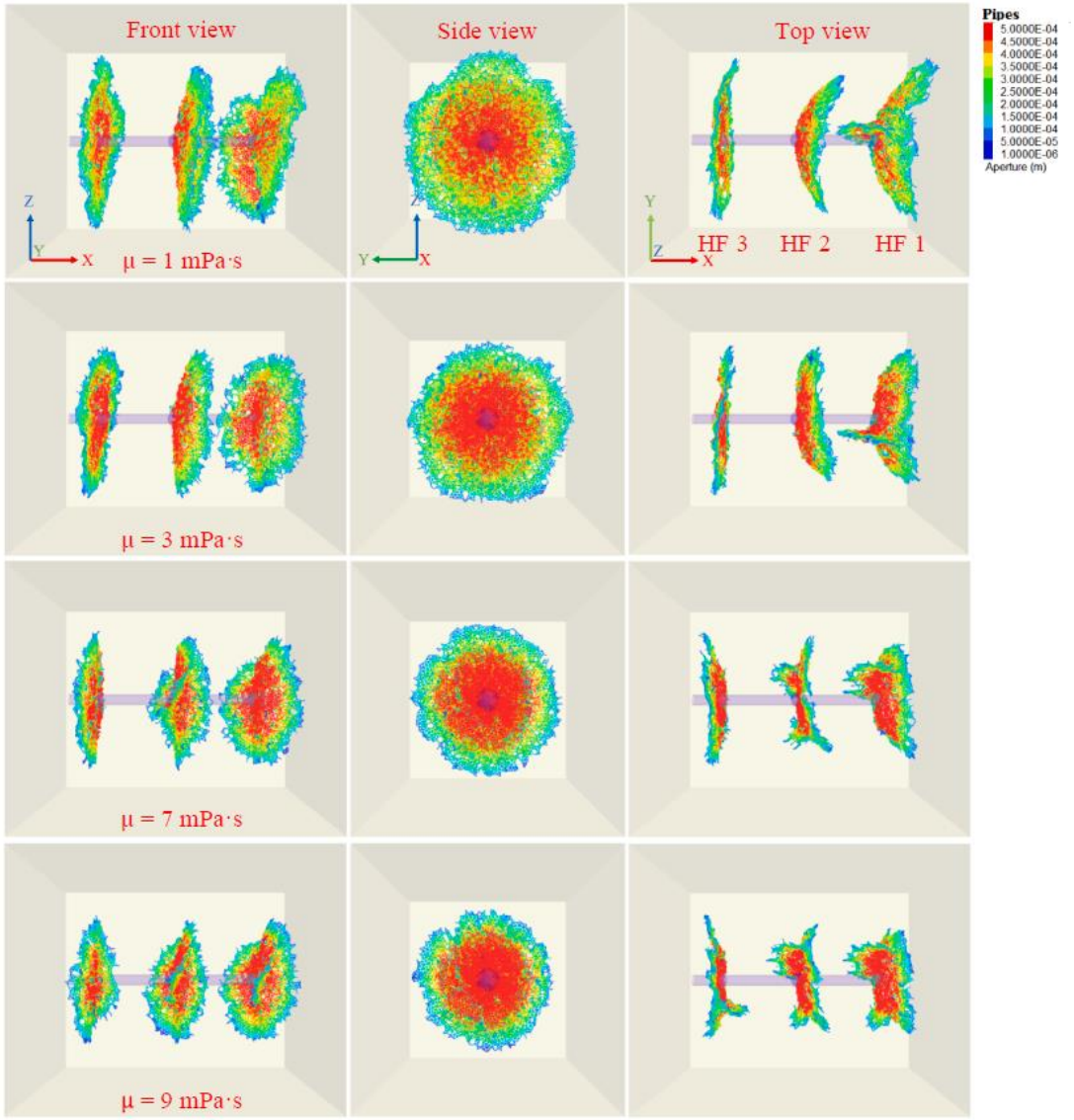

Fig. 9. Simultaneous growth of multiple HFs for varying fluid viscosity.

Fig. 10 present the horizontal profiles of multiple HFs for varying fluid viscosity. As shown in Fig. 10, the deflection angle for eachbranch has been measured. A high magnitude of fluid viscosity promotes the branching of hydraulic fractures. For the cases of 1 mPa·s and 3 mPa·s, the secondary fracture was induced in the vicinity

of the injection point. The secondary fracture tended to be perpendicular to the initial fracture plane. As for the cases of 7 mPa·s and 9 mPa·s, the branches were formed at the fracture tip. The branches are not aligned with the direction of principal stress. More branches can be observed in the case with higher fluid viscosity. In contrast, the propagation of secondary fracture in the vicinity of the injection point is inhibited.

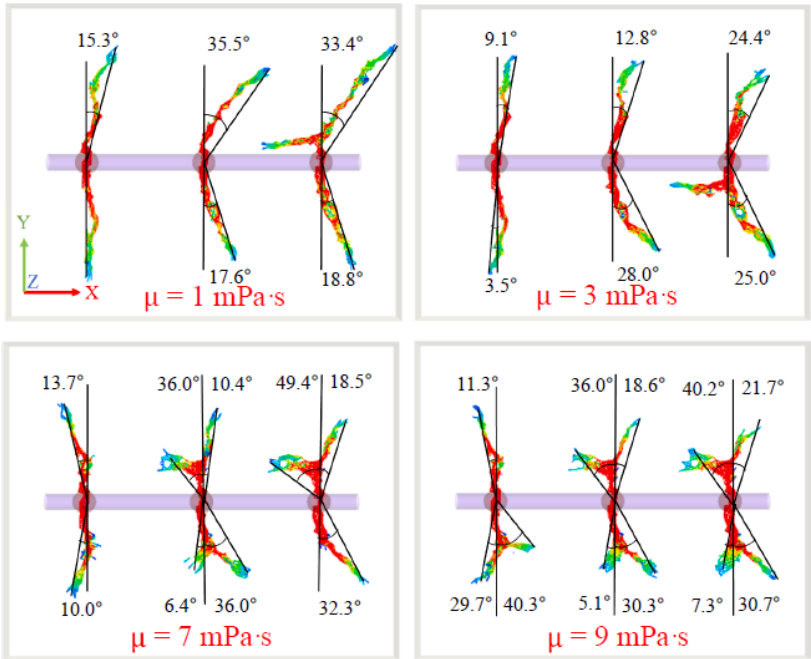

Fig. 10. Horizontal profiles of multiple HFs for varying fluid viscosity.

Fig. 11 shows the vertical growth and lateral growth of HF 3 with changes in fluid viscosity. It clear that the simulated HF size diminishing with the rise of fluid viscosity. As the fluid viscosity increased from 1 mPa·s to 9 mPa·s, the vertical growth reduced from 3.1 m to 2.37 m (- 0.73 m), and the lateral growth decreased by 0.71 m.

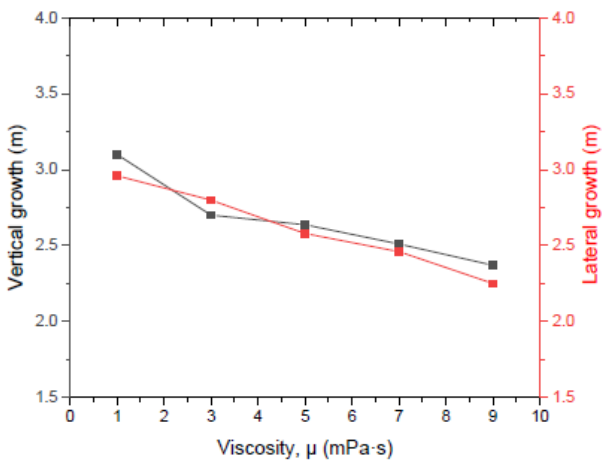

Fig. 11. Effect of fluid viscosity on the vertical and lateral growth of HF 3.

4.4. Effect of fluid injection rate

Four simulations were performed with injection rates (Q) of 0.001, 0.002, 0.006, and 0.008 m3/s, respectively. The volume of the injection fluid was assumed as 0.002 m3 for all models. Other parameters were assumed as: σx = σy = 5 MPa, σz = 7.5 MPa, E = 20 GPa, μ = 1 mPa·s.

When the injection rate was low (i.e., Q = 0.001 and 0.002 m3/s), only one secondary HF was simulated on HF 1. As the injection rate increased to a high level (i.e., Q = 0.006 and 0.008 m3/s), more branches developed on the primary HFs, as shown in Fig. 12.

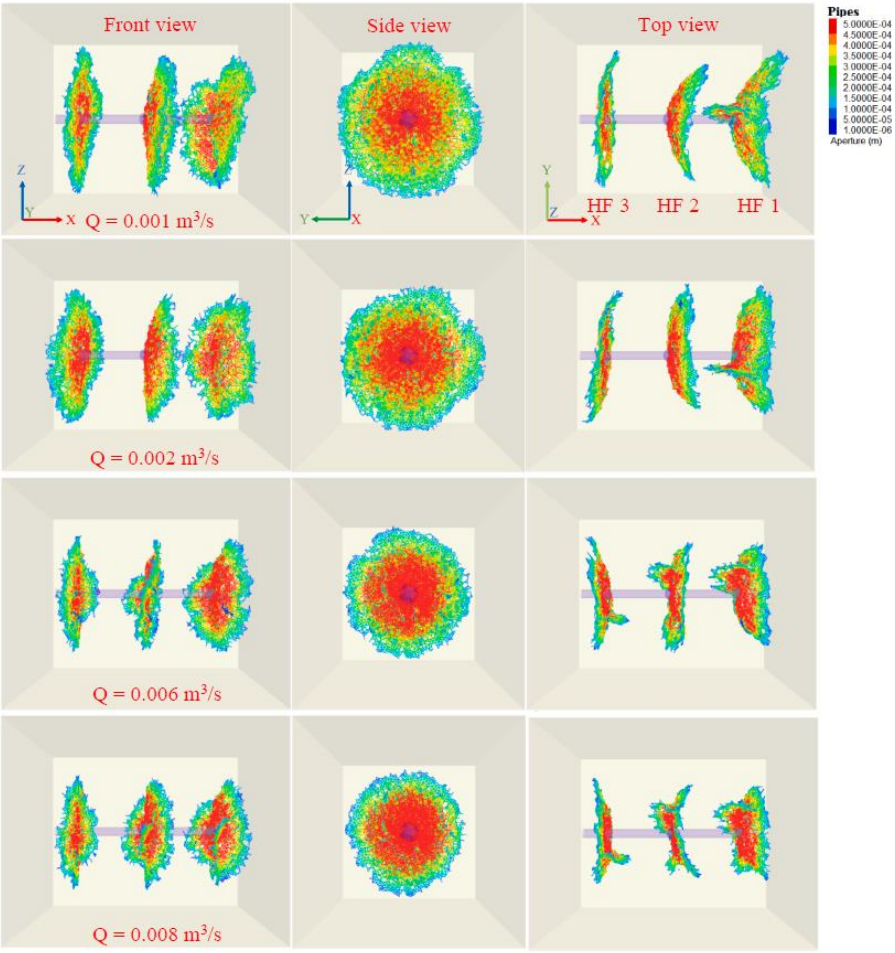

Fig. 12. Simultaneous growth of multiple HFs for varying fluid injection rates.

Specifically, each primary HF has one branch on it for the case of Q = 0.006 m3/s, with more than one branch developing on HF 2 and HF 3 for the higher injection rate case of Q = 0.008 m3/s. Note that with a low injection rate case of Q = 0.001 m3/s, the secondary HF formed in the vicinity of the injection point, whereas the branches simulated at a high injection rate case of Q = 0.008 m3/s formed at the tips of the primary HFs.

Fig. 13 present the horizontal profiles of multiple HFs for varying fluid injection rates. As shown in Fig. 13, the deflection angle for each branch has been measured. A high magnitude of fluid injection rate promotes the branching of hydraulic fractures. For the cases of Q = 0.001 m3/s and Q = 0.002 m3/s, the secondary fracture was induced in the vicinity of the injection point. The secondary fracture tended to be perpendicular to the initial

fracture plane. As for the cases of Q = 0.006 m3/s and Q = 0.008 m3/s, those branches were formed on the fracture tip. The branches are not aligned with the direction of principal stress.

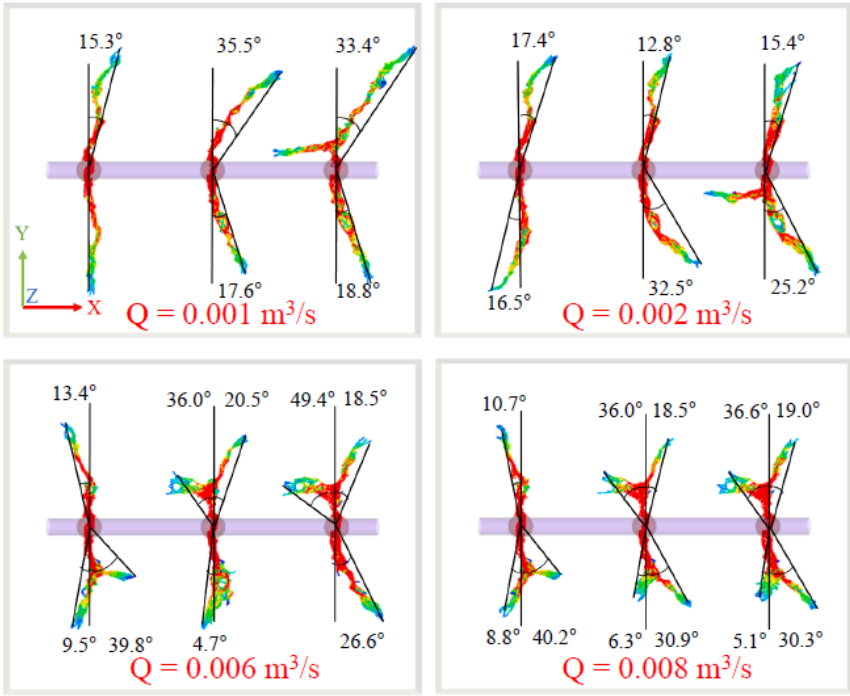

Fig. 13. Horizontal profiles of multiple HFs for varying injection rates.

Fig. 14 shows the vertical and lateral growth of HF 3 with changes in the fluid injection rate. The HF 3 size decreased with an increase in the injection rate for the same volume of injection. As the simulated injection rate is increased from 0.001 m3/s to 0.008 m3/s, the vertical HF growth decreased from 3.1 m to 2.47 m (- 0.63 m), and the lateral growth fell by 0.68 m.

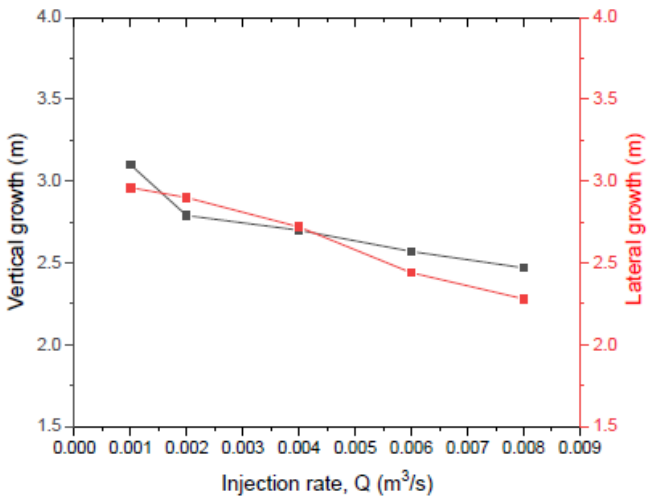

Fig. 14. Effect of fluid injection rate on the vertical and lateral growth of HF 3.

4.5. Multiple HFs propagation in a layered formation

Fig. 15 shows the propagation of multiple HFs in a layered formation. The volume of the rock block was assumed as 6 m × 5 m × 6 m. The Young's modulus in the outer layers for the two comparative models was assumed as 5 GPa, and 60 GPa, respectively. The middle layer had a thickness of 1.75 m and Young's modulus of 20 GPa. Other parameters were assumed as: σx = σy = 5 MPa, and σz = 7.5 MPa, μ = 1 mPa·s. The simulations were conducted under the condition of simultaneous fluid injection at a constant injection rate of 0.001 m3/s for 3 s.

It is clear from Fig. 15 that Young's modulus in adjacent layers had a significant effect on the vertical growth of the HFs. As Young's modulus of the adjacent layers increased from 5 GPa to 60 GPa, the vertical growth and the dimension of HFs were greatly enhanced.

For the case of an assumed modulus of E = 5 GPa in the adjacent layers, the HFs did not propagate beyond the middle layer. The vertical growth was restrained, therefore, fracture propagated laterally. Additionally, a fracture branch was simulated on HF 3. One wing of the inner fracture (HF 2) was deflected toward HF 3, potentially intersecting with it (see Fig. 15, top view). The other wing of the inner fracture was reoriented toward HF 1, resulting in an S-shaped geometry.

For the case of E = 60 GPa, substantial growth of HF was simulated in the adjacent layers. From the side view, it can be seen that the HFs near the boundary between layers exhibited a discontinuous propagation pattern. The HFs were relatively straight in the vertical direction in the middle layer. However, when the HFs grew into the high-modulus layer, the deflection/reorientation behavior became more pronounced. The outer primary HFs deviated away from the inner HF, exhibiting a bowl-shaped geometry. The inner HF 2 is characterized by a high degree of tortuosity. Despite the deviation in the propagation direction, the dominant propagation direction for HF 2 was in the direction of σz. The lateral growth of HF 2 was strongly affected by the interaction between adjacent HFs, which potentially reoriented or deflected into the σx direction (see the top view in Fig. 15). Additionally, the HF aperture in the high-modulus layer (E = 60 GPa) was in comparison smaller than that simulated in the middle layer (E = 20 GPa).

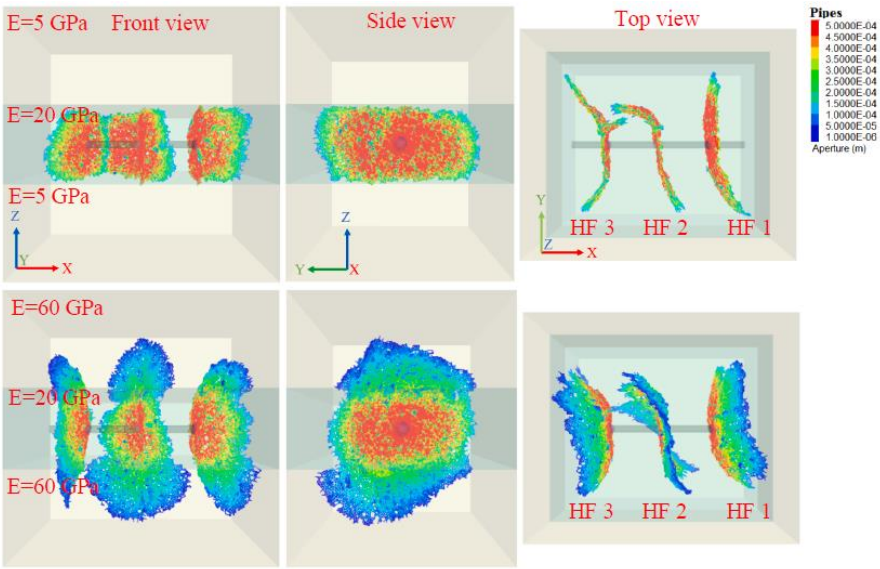

Fig. 15. The simultaneous growth of multiple HFs in a layered formation.

5. Discussion

A propagating HF alters the stress field near the HF, causing an increase in the local minimum principal stress. The increment of minimum horizontal stress may be greater than that of maximum horizontal stress, leading to a change in the direction of the maximum horizontal stress [17]. The induced stress field can have an impact on the further propagation of HFs. For the case of σx = σy = σz = 5 MPa (isotropic stress field), the propagating HF increased the compressive stress perpendicular to the HF plane, causing the deflection/reorientation of adjacent HFs. Because of the increment in the principal stress in the X-axis direction, the further propagation of HFs was along this direction. Thus, asymmetric non-planar HF surfaces were simulated, as shown in Fig. 4. The HFs have different curvatures as a result of non-symmetric compression induced by the adjacent opened HFs. Besides, these HFs were characterized by variable heights. Kresse and Weng [18] reported that stress shadows have a noticeable effect on the HF height growth and width profile. The height growth and width profile were calculated more accurately by including the 3D stress shadow effect. However, the pseudo-3D-based model failed to capture the deflection/reorientation behavior of HF propagation in a three-dimensional setting. The study presented in this paper highlights that the asymmetric non-planar propagation of HF, emphasizing the limitations of approaches assuming 2D plane strain and pseudo-3D models.

It is generally believed that the HF propagation pathway tends to be straighter with the presence of more significant differential stress [32]. For the case of σx = σy = 5 MPa, σz = 7.5 MPa, in our XSite models, a straighter HF plane was simulated than for the isotropic stress field case. Moreover, the secondary fracture was induced by the interaction between multiple HFs, which could represent another significant influence of the stress shadow effect. The stress shadow tends to cause changes in the direction and magnitude of the maximum and minimum horizontal stresses. Under specific conditions, an increase in the local minimum stress may result in secondary fracture growth in the orthogonal directions, as shown in Figs. 4 and 6.

As observed in Fig. 16, the primary fracture growth increases the stress normal to the HF plane. At some points, the increased principal stress orthogonal to the original propagation direction may exceed the principal stress in the original propagation direction. It may then become easiest for the HF to propagate in the direction orthogonal to the original direction leading to a secondary fracture being induced. The HF plane may flip back and forth between the two directions, as has been measured in actual fracturing practice [33].

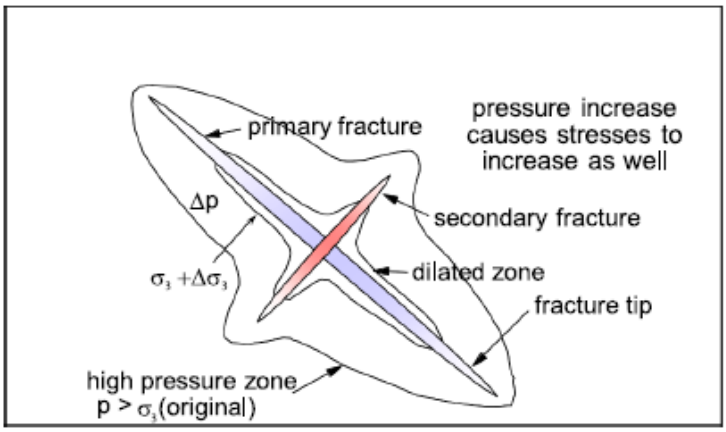

Fig.16. Near-field stresses altered by a fracture (After [33]).

In a thermal shock experiment [34], a secondary fracture (see the plane normal to the green arrows in Fig. 17) was induced on the inner primary fracture (the secondary fracture approximately orthogonal to the inner fracture). In addition, significant curving of the outer fracture is observed. The primary fracture on the right is diverted away from the inner primary fracture due to the induced stresses, resulting in a non-planar geometry. This phenomenon has been successfully captured in the XSite simulations.

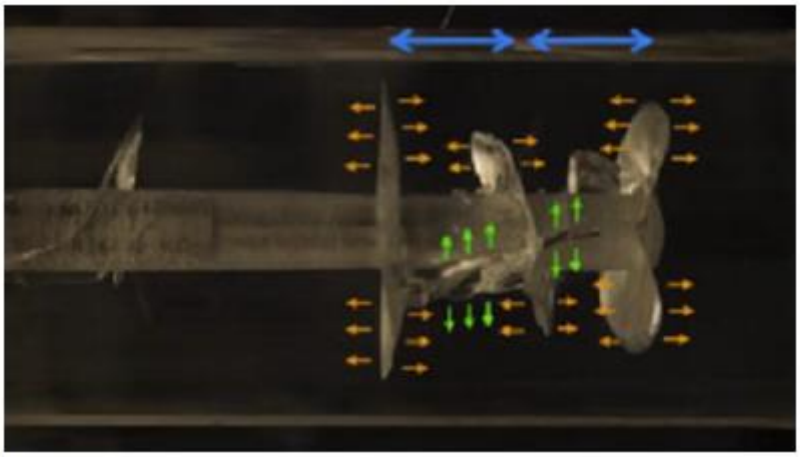

Fig. 17. Morphology of multiple fractures generated from cryogenic thermal shock (After [34]).

Fisher et al. concluded that an increase in the local minimum stress magnitude tends to inhibit the initiation of adjacent HFs and encourage HF growth in orthogonal directions [1]. Moreover, the formation of orthogonal HFs may contribute to productivity as the network size and network density are both enhanced by the growth of orthogonal HFs.

Higher Young's modulus could amplify the interaction of multiple HFs. In the formation with an assumed higher modulus, more secondary HFs were simulated, and strong curving of primary HFs can be observed (see Fig. 6). Note that the fluid flow is fully coupled with mechanical deformation. The aperture of the HF in the stiff layer was smaller than that in the soft layer. In contrast, the dimensions of the HF in the stiff layer were greater than those in the soft layer, assuming a uniform injection rate. The variation in modulus had an impact on the gradient of induced stress and on the HF propagation path. Therefore, the interaction between multiple HFs was amplified, and more secondary HFs occurred with a higher Young's modulus. Besides, strong curving of primary HFs can be found in the case of high modulus, as shown in Fig. 6. As reported in the previous publication, the reorientation of an HF is more likely to occur in the formation with high Young's modulus, and varying modulus can result in a variation in the range of net closure pressure [35].

As shown in Fig. 15, the high modulus encouraged the HF to cross the boundary into adjacent layers, whereas the lower modulus hindered the HF propagation. Two explanations have been proposed concerning the effect of modulus contrast between adjacent layers on the simulated HF height containment. First, the stiff layer serves as a barrier to inhibit HF propagation as it initiates from a soft layer and propagate towards the adjacent stiff layer. The stress intensity factor (SIF) is reduced to zero as the HF tip propagates from the soft layer to the stiff layer. In contrast, the SIF increases to infinity as the HF tip propagates from the stiff layer to the soft layer [36,37]. HF growth in width is reduced in the stiff layer, constraining the fluid flow into the HF tip. Thus, the adjacent stiff

layer will limit the growth of HFs under the condition of constant pressure within the HF [38]. The second explanation is that the stiff layer is conducive to the HF propagation from a soft layer into the stiff layer. The SIF will be enhanced after the HF tip crosses the boundary into the stiff layer [39]. The SIF will be reduced after the HF tip crosses the boundary into the soft layer [40]. Because of the hydro-mechanical coupling effect, the dimensions of the HF in the stiff layer will be larger than those in the soft layer [39]. The two proposed explanations are somewhat controversial as the condition of the fracture-spanning boundary has been not considered in fracture mechanics solutions, and the hydro-mechanical coupling effect was not included in traditional numerical models.

The modulus contrast in a layered formation has a remarkable effect on the interaction between multiple HFs. When the layer has a low modulus, the HF height will be constrained, whereas the lateral growth may be relatively enhanced. At some points, the stress shadow effect may be enhanced within the middle layer (i.e., secondary HF and highly curved HF path). The fracture path in the vertical direction is relatively straight. In the high-modulus adjacent layer, strong curving on the HF surface can be observed. Thus, a high degree of tortuosity of the HF path in the vertical direction can be expected. Note that the bedding planes, which are commonly observed in layered formations, were not included in the present models. The presence of geological discontinuities will affect HF propagation during fracturing treatment [41,42]. In future work, efforts will be made to include the interaction between discontinuities and HFs in the presence of stress shadows.

A higher magnitude of flow resistance will be introduced in treatment with higher viscosity fluids. In turn, the induced stress in the rock will be more pronounced with higher viscosity fluid treatments. Strong stress concentration around the HF tip can be expected, which has the potential to induce the failure of the rock. Therefore, more branches were simulated on the primary HFs for higher fluid viscosity cases (see Fig. 9). Similarly, the injection of fluid at a higher injection rate has a higher energy magnitude. Strong stress concentration around the HF tip was induced with the treatment of high injection rate fluid, potentially causing the branching at the front of the primary HF (see Fig. 12). In summary, the dominant mechanism accounting for the branching at the tips of the primary HF may not be the effect of the stress shadow but the strong stress concentration around the HF tip (note that the stress shadow effect still exists). The multiple HFs amplify the increase in the minimum principal stress in the inter-fracture region. With a low magnitude of fluid viscosity/injection rate, the secondary HF was formed close to the injection point due to the additive increase in the minimum principal stress. However, the branching formed at the front of the primary HF under a high magnitude of fluid viscosity/injection rate may be attributed to the strong stress concentration around the HF tip.

Stress intensity factors and energy release rates increase before branching then drop since energy is now used to propagate two branches [43]. If cracks are branching it indicates that the stress is high and the material is unable to dissipate the energy that is driving the failure with a single crack. High-energy release (and high stress in the part) will cause many branches of the crack [44]. In atomistic models, under conditions that lead to instability of the crack path, cracks can branch without a specific criterion[45]. Note that understanding the various mechanisms governing the fracture branching remains a challenge. Exhaustive modeling of all the previously mentioned mechanisms would certainly require a more sophisticated simulator.

The stress shadow effect is influenced by multiple factors, including stress anisotropy, and hydraulic pressure, aspect ratio, Poisson's ratio, among others [46]. These factors can act together to describe the interaction between multiple fractures. The determination of which factor dominates is a complex problem. Furthermore, a stress shadow is the result of a dynamic process that evolves with the propagation of HFs. The stress field around the fracture changes with the propagation of HFs. In turn, the continued propagation (e.g., deflection or branching) of a simulated HF was affected by the local stress variation. The dynamic evolution of a stress shadow poses a challenge to the suitability of a simplified analytical solution. Although numerous numerical models have been developed for simulating the propagation of HFs, few studies have been undertaken to study the interaction between multiple HFs in a three-dimensional setting. The overall propagation of an HF depends on the competition between lateral, upward, and downward HF growth [47]. Additionally, both the differential stresses between σ2 and σ3 and between σ1 and σ3 impact the HF reorientation trajectory [48]. Numerical simulation based on a 2D plane strain approach or pseudo-3D models cannot correctly represent a 3-D fracture system. Three-dimensional non-planar propagation and the branching behavior of HFs must be considered. The robust simulators that account for fluid flow, solid deformation, HF propagation, and their interaction, in a fully-coupled setting, are essential for the realistic prediction of the dynamic interaction between HFs.

Although numerical analysis has made a significant contribution to capturing the propagation of HF, it remains an approximation of the real physical process. Moreover, the complexity of fractured rock mass is challenging to be incorporated into a numerical model. Methodologies, analysis, and field experiments are required to confirm or calibrate the numerical result. For instance, Pettitt et al. [49] presented the fracture network engineering (FNE) method. In this method, the integrated application of numerical modeling with enhanced microseismic analysis provides a feedback loop, in which numerical modeling is enhanced and constrained by the information provided by the microseismic data. The numerical model provides one promising tool to investigate the dynamic interaction between multiple HFs, potentially integrating microseismic field mapping and other data into the optimization of the fracture treatment.

6. Conclusion

account for the effects of in-situ stresses, Young's modulus, the viscosity of the fluid, and the injection rate. The propagation of multiple HFs in a layered formation is also simulated. The following conclusions can be drawn.

(1) The interaction of multiple fractures can alter the local stress field, which in turn affects fracture propagation. Simultaneous propagating fractures may grow toward or away from each other, resulting in complicated non-planar geometry and branching on fractures. The dominant fractures tend to propagate parallel to the direction of maximum principal stress.

(2) High Young's modulus will amplify the interaction between adjacent fractures. More secondary fractures normal to the initial fracture plane and a greater dimension of fracture can be expected when fracturing in formations with high Young's modulus.

(3) Treatment with a higher fluid viscosity /injection rate contributes to the branching at the tips of the primary fracture. In contrast, the propagation of secondary fracture in the vicinity of the injection point is inhibited.

(4) An adjacent layer with a high modulus promotes the propagation of fractures. With the presence of the adjacent layers with low modulus, the fracture height will be constrained, whereas the lateral growth will be in contrast relatively promoted.

Declaration of Competing Interest

The authors declare that they have no known competing financial interests or personal relationships that could have appeared to influence the work reported in this paper.

Acknowledgments

We thank Dr. Branko Damjanac at Itasca Consulting Group, Inc. for providing XSite used for the modeling and the guidance of the HF modeling. The first author wishes to thank the China Scholarship Council for their support for visiting Simon Fraser University. This work has been supported by the National Key Research and Development Program of China (grant no. 2017YFC0603003).

References

[1] Fisher MK, Heinze JR, Harris CD, Davidson BM, Wright CA, Dunn KP. Optimizing horizontal completion techniques in the Barnett shale using microseismic fracture mapping. SPE Annu Tech Conf Exhib Soc Petroleum Eng 2004. https://doi.org/10.2118/90051-MS.

[2] Abuaisha M, Loret B, Eaton D. Enhanced Geothermal Systems (EGS): Hydraulic fracturing in a thermo–poroelastic framework. J Pet Sci Eng 2016;146. https:// doi.org/10.1016/j.petrol.2016.07.027.

[3] Lyu S, Wang S, Chen X, Wang S, Wang T, Shi X, et al. Natural fractures in soft coal seams and their effect on hydraulic fracture propagation: A field study. J Pet Sci Eng 2020;192:107255. https://doi.org/10.1016/j.petrol.2020.107255.

[4] Green AE, Sneddon IN. The distribution of stress in the neighbourhood of a flat elliptical crack in an elastic solid. Math Proc Cambridge Philos Soc 1950;46: 159–63. https://doi.org/10.1017/S0305004100025585.

[5] Warpinski NR, Wolhart SL, Wright CA. Analysis and prediction of microseismicity induced by hydraulic fracturing. SPE J 2004;9:24–33. https://doi.org/10.2118/87673-PA.

[6] Liebowitz H. Fracture. An advanced treatise. Vol. II: Mathematical fundamentals 1968.

[7] Zhou J, Zeng Y, Jiang T, Zhang B. Laboratory scale research on the impact of stress shadow and natural fractures on fracture geometry during horizontal multi- staged fracturing in shale. Int J Rock Mech Min Sci 2018;107:282–7. https://doi.org/10.1016/j.ijrmms.2018.03.007.

[8] Bunger AP, Jeffrey RG, Kear J, Zhang X, Morgan M. Experimental investigation of the interaction among closely spaced hydraulic fractures. 45th US Rock Mech/ Geomech Symp 2011.

[9] Weng X, Kresse O, Chuprakov D, Cohen CE, Prioul R, Ganguly U. Applying complex fracture model and integrated workflow in unconventional reservoirs. J Pet Sci Eng 2014;124:468–83. https://doi.org/10.1016/j.petrol.2014.09.021.

[10] Dahi Taleghani A, Gonzalez M, Shojaei A. Overview of numerical models for interactions between hydraulic fractures and natural fractures: Challenges and limitations. Comput Geotech 2016;71:361–8. https://doi.org/10.1016/j.compgeo.2015.09.009.

[11] Lecampion B, Bunger A, Zhang X. Numerical methods for hydraulic fracture propagation: A review of recent trends. J Nat Gas Sci Eng 2018;49:66–83. https:// doi.org/10.1016/j.jngse.2017.10.012.

[12] Salimzadeh S, Usui T, Paluszny A, Zimmerman RW. Finite element simulations of interactions between multiple hydraulic fractures in a poroelastic rock. Int J Rock Mech Min Sci 2017;99:9–20. https://doi.org/10.1016/j.ijrmms.2017.09.001.

[13] Haddad M, Sepehrnoori K. XFEM-based CZM for the simulation of 3D multiple-cluster hydraulic fracturing in quasi-brittle shale formations. Rock Mech Rock Eng 2016;49:4731–48. https://doi.org/10.1007/s00603-016-1057-2.

[14] Olson JE, Taleghani AD. Modeling simultaneous growth of multiple hydraulic fractures and their interaction with natural fractures. SPE Hydraul Fract Technol Conf Soc Petroleum Eng 2009:726–32. https://doi.org/10.2118/119739-MS.

[15] Eberhardt E, Stead D, Stimpson B, Lajtai EZ, Engineering G. The effect of neighbouring cracks on elliptical crack initiation and propagation in uniaxial and triaxial stress fields 1998;59:103–15. doi:10.1016/s0013-7944(97)00095-7.

[16] Bunger AP, Zhang X, Jeffrey RG. Parameters affecting the interaction among closely spaced hydraulic fractures. SPE J., vol. 17, Society of Petroleum Engineers; 2012, p. 292–306. doi:10.2118/140426-PA.

[17] Wu K, Olson JE. Simultaneous multifracture treatments: Fully coupled fluid flow and fracture mechanics for horizontal wells. SPE J 2015;20:337–46. https:// doi.org/10.2118/167626-PA.
[18] Kresse O, Weng X. Numerical modeling of 3D hydraulic fractures interaction in complex naturally fractured formations. Rock Mech Rock Eng 2018;51:3863–81. https://doi.org/10.1007/s00603-018-1539-5.
[19] Kang H, Li J, Yang J, Gao F. Investigation on the influence of abutment pressure on the stability of rock bolt reinforced roof strata through physical and numerical modeling. Rock Mech Rock Eng 2017;50:387–401. https://doi.org/10.1007/s00603-016-1114-x.
[20] Stead D, Eberhardt E, Coggan JS. Developments in the characterization of complex rock slope deformation and failure using numerical modelling techniques. Eng Geol 2006;83:217–35. https://doi.org/10.1016/j.enggeo.2005.06.033.
[21] Elmo D, Stead D. An integrated numerical modelling-discrete fracture network approach applied to the characterisation of rock mass strength of naturally fractured pillars. Rock Mech Rock Eng 2010;43:3–19. https://doi.org/10.1007/s00603-009-0027-3.
[22] Zangeneh N, Eberhardt E, Bustin RM. Investigation of the influence of stress shadows on horizontal hydraulic fractures from adjacent lateral wells. J Unconv Oil Gas Resour 2015;9:54–64. https://doi.org/10.1016/j.juogr.2014.11.001.
[23] Nagel NB, Sanchez-Nagel MA, Zhang F, Garcia X, Lee B. Coupled numerical evaluations of the geomechanical interactions between a hydraulic fracture stimulation and a natural fracture system in shale formations. Rock Mech Rock Eng 2013;46:581–609. https://doi.org/10.1007/s00603-013-0391-x.
[24] Gao F, Kaiser PK, Stead D, Eberhardt E, Elmo D. Numerical simulation of strainbursts using a novel initiation method. Comput Geotech 2019;106:117–27. https://doi.org/10.1016/j.compgeo.2018.10.018.
[25] Gao FQ, Stead D. The application of a modified Voronoi logic to brittle fracture modelling at the laboratory and field scale. Int J Rock Mech Min Sci 2014;68: 1–14. https://doi.org/10.1016/j.ijrmms.2014.02.003.
[26] Damjanac B, Detournay C, Cundall PA. Application of particle and lattice codes to simulation of hydraulic fracturing. Comput Part Mech 2016;3:249–61. https://doi.org/10.1007/s40571-015-0085-0.
[27] Liu X, Qu Z, Guo T, Sun Y, Wang Z, Bakhshi E. Numerical simulation of non-planar fracture propagation in multi-cluster fracturing with natural fractures based on Lattice methods. Eng Fract Mech 2019;220:106625. https://doi.org/10.1016/j.engfracmech.2019.106625.
[28] Fu W, Bunger AP. 3D DEM simulation on the interference of multiple hydraulic fractures in horizontal wells. 53rd US Rock Mech Symp. 2019.
[29] Damjanac B, Detournay C, Cundall P. Numerical simulation of hydraulically driven fractures. Model. Rock Fract. Process., Cham: Springer International Publishing; 2020, p. 531–61. doi:10.1007/978-3-030-35525-8_20.
[30] Cundall PA. Lattice method for modeling brittle , jointed rock. 2nd Int. FLAC/DEM Symp. Contin. distinct Elem. Numer. Model. geo-mechanics, Melbourne, Australia: 2011.
[31] Damjanac B, Detournay C, Cundall P, Purvance MHJ. XSite-description of formulation. Minneapolis: Itasca Consulting Group, Inc.; 2011.
[32] Zhang X, Jeffrey RG, Bunger AP, Thiercelin M. Initiation and growth of a hydraulic fracture from a circular wellbore. Int J Rock Mech Min Sci 2011;48:984–95.
https://doi.org/10.1016/j.ijrmms.2011.06.005.
[33] Dusseault MB. Lecture notes provided at a short course. Used with permission of the author. 2019.
[34] Wu Y-S, Yin X, Kneafsey T, Miskimins J, Wang L, Cha M, et al. Development of non-contaminating cryogenic fracturing technology for shale and tight gas reservoirs. Project Number : 10122-20. 2016.
[35] Roussel NP, Manchanda R, Sharma MM. Implications of fracturing pressure data recorded during a horizontal completion on stage spacing design. Soc Pet Eng - SPE Hydraul Fract Technol Conf 2012 2012:794–807. https://doi.org/10.2118/152631-ms.
[36] Simonson ER, Abou-Sayed AS, Clifton RJ. Containment of massive hydraulic fractures. Soc Pet Eng J 1978;18:27–32. https://doi.org/10.2118/6089-PA.
[37] Thiercelin M, Roegiers J, Boone TJ, Ingraffea AR. An investigation of the material parameters that govern the behavior of fractures approaching rock interfaces. In: 6th ISRM Congr 1987; 1987. p. 263–9.
[38] van Eekelen HAM. Hydraulic fracture geometry: fracture containment in layered formations. Soc Pet Eng J 1982;22:341–9. https://doi.org/10.2118/9261-PA. [39] Gu H, Siebrits E. Effect of formation modulus contrast on hydraulic fracture height containment. SPE Prod Oper 2008;23:170–6.
[40] Huang J, Fu P, Settgast RR, Morris JP, Ryerson FJ. Evaluating a simple fracturing criterion for a hydraulic fracture crossing stress and stiffness contrasts. Rock Mech Rock Eng 2019;52:1657–70. https://doi.org/10.1007/s00603-018-1679-7.
[41] Rogers S, Elmo D, Dunphy R, Bearinger D. Understanding hydraulic fracture geometry and interactions in the Horn River Basin through DFN and numerical modeling. Soc Pet Eng - Can Unconv Resour Int Pet Conf 2010;2010(2):1426–37.
[42] Zhao K, Stead D, Kang H, Damjanac B, Donati D, Gao F. Investigating the interaction of hydraulic fracture with pre-existing joints based on lattice spring modeling. Comput Geotech 2020;122:103534. https://doi.org/10.1016/j.compgeo.2020.103534.
[43] Ravi-Chandar K. Dynamic Fracture. Elsevier 2004. https://doi.org/10.1016/B978-0-08-044352-2.X5000-5.
[44] Hayes MD, Edwards DB, Shah AR. Fractography Basics. Fractography Fail Anal Polym Elsevier 2015:48–92. https://doi.org/10.1016/b978-0-323-24272- 1.00004-0.

[45] Zhou SJ, Lomdahl PS, Thomson R, Holian BL. Dynamic crack processes via molecular dynamics. Phys Rev Lett 1996;76:2318–21. https://doi.org/10.1103/ PhysRevLett.76.2318.
[46] Taghichian A, Zaman M, Devegowda D. Stress shadow size and aperture of hydraulic fractures in unconventional shales. J Pet Sci Eng 2014;124:209–21. https://doi.org/10.1016/j.petrol.2014.09.034.
[47] Salimzadeh S, Hagerup ED, Kadeethum T, Nick HM. The effect of stress distribution on the shape and direction of hydraulic fractures in layered media. Eng Fract Mech 2019;215:151–63. https://doi.org/10.1016/j.engfracmech.2019.04.041.
[48] He Q, Suorineni FT, Ma T, Oh J. Effect of discontinuity stress shadows on hydraulic fracture re-orientation. Int J Rock Mech Min Sci 2017;91:179–94. https:// doi.org/10.1016/j.ijrmms.2016.11.021.
[49] Pettitt W, Pierce M, Damjanac B, Hazzard J, Lorig L, Fairhurst C, et al. Fracture network engineering for hydraulic fracturing. Lead Edge 2011;30:844–53. https://doi.org/10.1190/1.3626490.